Master Thesis, Department of Geosciences

Separation of reflections from diffractions using the CRS-technique

by

Muhammad Waqas Javed

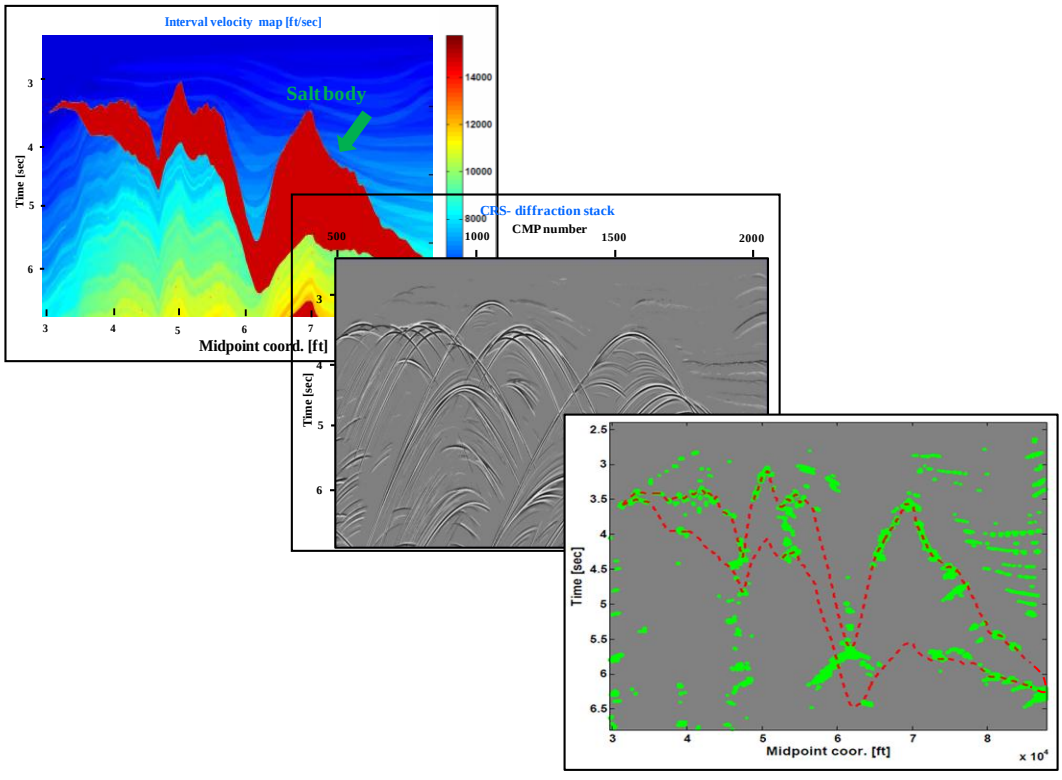

UNIVERSITY OF OSLO

FACULTY OF MATHEMATICS AND NATURAL SCIENCES

Separation of reflections from diffractions using the CRS-technique

by

Muhammad Waqas Javed

Master Thesis in Geosciences

Discipline: Petroleum Geology and Petroleum Geophysics

Department of Geosciences

Faculty of Mathematics and Natural Sciences

University of Oslo

June, 2012

Tutor: Professor Leiv-J. Gelius (UiO)
This work is published digitally through DUO – Digitale Utgivelser ved UiO
http://www.duo.uio.no
It is also catalogued in BIBSYS (http://www.bibsys.no/english)

Acknowledgements

I feel instigated from within to extend my steadfast thanks to ALMIGHTY ALLAH whose magnanimous and chivalrous blessings enabled me to perceive and purse my ambitions and objectives. Special praises to Prophet Muhammad (PBUH), who is bellwether for humanity as a whole.

I express special appreciation to my supervisor Professor Leiv-J. Gelius for his invaluable input and thought-provoking discussions during this present study. He has been tremendously supportive in shaping my thoughts to carry out this work within the time frame.

I also extend my special thanks to Phd Student Endrias Getachew Asgedom for his esteemed guidance, suggestions, discussion and professional support throughout my thesis work.

Special thanks to my friends; especially JAN GROUP from University of Oslo for providing me confidence and helps me in my education and other matters.

In the end my whole hearted and incessant gratitude to my loving parents, my brothers and my sisters, who always appreciated, encouraged, and helped me during my eighteen years of studies.

Javed, M., W.

01.06.2012

Abstract

Seismic data contains reflections along with diffractions. Diffractions in seismic data are related to different features like faults, fractures, pinchouts and rough edges of salt bodies. It follows that suppression of reflections and enhancement of diffractions can be very useful for seismic interpretation of various subsurface features that cause diffractions. During the last years, different techniques have been proposed to separate reflections from diffractions. In this study both simple synthetic test data and complex synthetic data (Sigsbee2a) have been used to investigate the modified version of the Common Reflection Surface (CRS) technique. The simple synthetic data were sorted into different domains to investigate the difference in signature of reflections and diffractions. A two-step procedure based on CMP-sorting followed by zero-offset (eventually constant-offset) sorting seemed to give a good diffraction separation. Optimal parameters were determined based on Semblance as a coherency measure. This separation scheme was applied to a complex controlled data set (Sigsbee2a) and diffractions were successfully separated from reflections.

Contents

Chapter 1 MOTIVATION AND INTRODUCTION

Diffractions in seismic signal processing carry information about objects smaller than the seismic wavelength like parts of faults, near surface scattering objects, pinch outs, wedge outs, reef edges or any abrupt change in facies (Kanasewich and Phadke, 1988; Moser and Howard, 2008). In general, diffractions are treated as noise in the petroleum industry since they mostly have a weak strength. Seismic imaging has therefore been geared toward specular reflections. The motivation behind separating diffractions from reflections is that diffraction images provide higher resolution information to the interpreter since small but essential structural details are enhanced (Khaidukov et al., 2004).

In recent years, various ways to separate reflections from diffractions have been proposed followed by higher resolution imaging. For example, by using plane wave destruction filters after stacking, a depth image of diffractions can be obtained (Fomel, 2002; Fomel et al., 2007). Landa et al. (1987) successfully suppressed reflections and enhanced diffractions in the common offset domain by employing the double-square-root traveltime moveout. Asgedom et al. (2011 a) used the Common Reflection Surface (CRS) technique to separate reflections from diffractions. In the present study we will further investigate this latter approach.

The thesis is organized as follows. In Chapter 2, we show how the conventional common mid-point (CMP) analysis and the common reflection surface (CRS) analysis are related to each other. The CRS technique is originally developed for reflection data. We show how the method can be extended to the case of diffractions and present the CRS parameters to be determined. The optimal set of such parameters is found using a coherency measure like Semblance. In Chapter 3, simple synthetic data are generated for a reflector and a nearby diffractor. By considering these data in different domains one obtains an idea on how to sort data in order to obtain optimal separations. Chapter 4 gives a demonstration of how well the CRS-technique separates diffractions from reflections using the simple test data from Chapter 3. In Chapter 5, the complex synthetic Sigsbee2a dataset is employed to test the feasibility of

this modified CRS-technique. Diffractions associated with the boundaries of the complex salt body are shown to be successfully enhanced and separated. Finally, Chapter 6 discusses the overall work and gives a set of main conclusions.

Chapter 2 THE CRS CONCEPT – BASIC THEORY

2.1. CMP AND CRS COMPARISON

Common mid-point gather (CMP) analysis is a conventional way to stack seismic data within each individual CMP gather. The traveltime equation for reflections associated with a horizontal reflector is used in Common mid-point gather (CMP) analysis (Eq. 3.1).

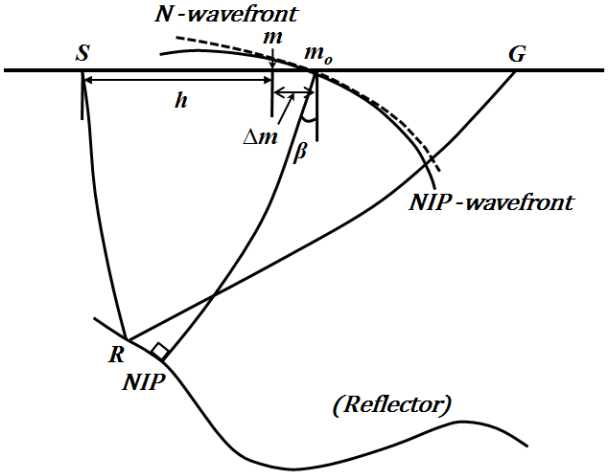

Fig. 2.1. *Source-receiver pair around the central ray at* $\boldsymbol{m_o}$ *with CRS parameters (modified from Asgedom et al. (2011 c)).*

Consider reflections from an arbitrary reflector (Fig. 2.1). We introduce now the concept of a zero-offset central ray and the paraxial approximation to obtain a travel time expression for a nearby ray with a given offset. This new travel time Eq. (2.1) represents a generalization of Eq. (3.1) where also the midpoint-coordinate can be varied. To properly take into account the shape of the reflector, new parameters have to be introduced like the local slope of the traveltime curve and its curvature. The curvature move-out velocity V_{CMO} in Eq. (2.1) is dependent upon the curvature unlike the NMO velocity (Mann et al., 2007).

$$t^2(\Delta m,\ h) = t_o^2 + \frac{h^2}{v_{NMO}^2} + \frac{\Delta m^2}{v_{CMO}^2} + 4\, t_o\, p\Delta m + 4\, p^2 \Delta m^2 \qquad (2.1)$$

where $\Delta m = m - m_o$ is the relative mid-point coordinate and p is the horizontal slowness or gradient (Mann et al., 2007). The Common-Reflection-Surface (CRS) technique makes use of Eq. (2.1) to stack data along both midpoint and offset coordinates unlike conventional CMP stacking. The CRS technique can increase the signal to noise ratio but is more complex than the conventional CMP stacking. Both CMP and CRS stacking depend upon the continuity of the reflector (Mann et al., 2007).

2.2. CRS TECHNIQUE FOR REFLECTIONS

We can rewrite Eq. (2.1) describing the hyperbolic moveout (t) for reflections as follows:

$$t^2(\Delta m,\ h) = [\, t_o + A\, \Delta m]^2 + B\, \Delta m^2 + C\, h^2 \qquad (2.2a)$$

where Δm is relative midpoint coordinate, h is the half-offset and t_o is the zero-offset traveltime (Asgedom et al., 2011 a). Parameters A , B and C are calculated for the central ray at m_o. If we compare Eq. (3.1) and Eq. (2.1), it is clear that the CRS technique represents an extension of the conventional CMP stacking technique to include also neighbouring CMP gathers.

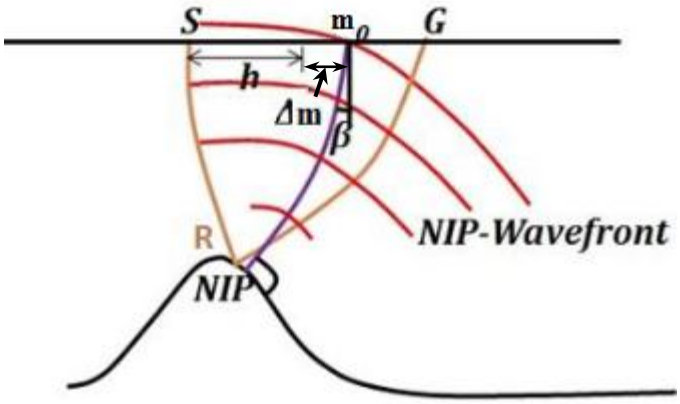

(a)

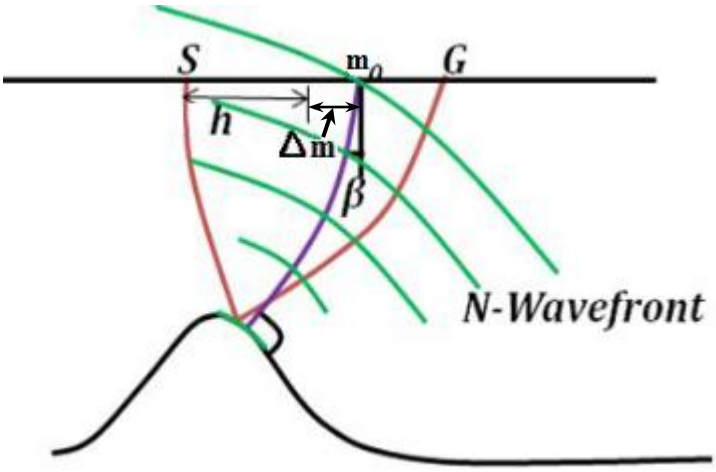

(b)

Fig. 2.2. *Definitions of NIP (normal incident point) wavefront (a) and N (normal) wavefront (b) (modified from Asgedom et al. (2011 c)).*

The CRS parameters A, B and C can be determined from the take-off angle β of the central ray and two associated wavefronts. One is the NIP (normal incident point) wavefront associated with a point source at the reflection point of the central ray (Fig. 2.2a). The other is the N (normal) wavefront associated with an exploding reflection segment (Fig. 2.2b) (Asgedom et al., 2011 b).

Explicit expressions for the parameters A, B and C are as follows, (v_o being medium velocity at surface) (Jager et al., 2001):

$$A = \frac{2\sin\beta}{v_o}, B = \frac{2\,t_o\,cos^2\,\beta\,K_N}{v_o}\,, C = \frac{2\,t_o\,cos^2\,\beta\,K_{NIP}}{v_o} \tag{2.2b}$$

2.3. CRS TECHNIQUE FOR DIFFRACTIONS

In case of diffractions, reflectors shrink into points and the NIP and N-waves become identical (Zhang et al., 2001). For this special case, the parameter B is equal to parameter C (Asgedom et al., 2011 a) and Eq. (2.2a) simplifies to

$$t^2(\Delta m,\ h) = [\,t_o + A\,\Delta m]^2 + C\,[\Delta m^2 + h^2] \tag{2.3}$$

Thus equations (2.2a) and (2.3) suggest that reflections and diffractions have different traveltime curves (Asgedom et al., 2011 a).

2.4. CRS PARAMETERS

The CRS parameters are determined using a two-step procedure:

i) First the data are sorted in CMP-gathers. This implies setting $\Delta m = 0$ in Eq. (2.3) which gives the simplified CRS-equation for diffractions in the CMP-domain:

$$t^2(m_o, h) = {t_o}^2 + C\, h^2 \tag{2.4}$$

Thus, the parameter C can now be determined from a conventional velocity analysis. In case of a layered Earth we will have $C = \frac{4}{v_{rms}^2}$.

ii) Secondly data are stacked and a zero-offset section is formed. Consequently, the CRS-equation for diffractions takes the form (follow from Eq. (2.3) by setting $h = 0$):

$$t^2(\Delta m, 0) = [\, t_o + A\, \Delta m]^2 + C\, \Delta m^2 \tag{2.5}$$

Parameter A is now determined by stacking data within the stack (user defined aperture).

In order to determine optimal parameters a coherency measure needs to be applied. Such a measure (Semblance) will be discussed in section 2.5.

2.5 COHERENCY MEASURE (SEMBLANCE)

Within a time analysis window, the measure of trace to trace similarity is denoted coherencey (Gelius and Johansen, 2010). Usually, the coherency of a seismic dataset is characterized by Semblance (Asgedom et al., 2011 a). For a given sample k at a given (reference) trace Semblance can mathematically be written in the form (Kirlin, 1992):

$$\boldsymbol{S} = \frac{\mathbf{1}}{\boldsymbol{M}} \frac{\sum_{j=k-N/2}^{J=k+N/2} \left|\sum_{i=1}^{M} x(j,i)\right|^2}{\sum_{j=k-N/2}^{j=k+N/2} \sum_{i=1}^{M} |x(j,i)|^2} \tag{2.6}$$

Here, Semblance is computed for N samples taken from M traces in a window (*cf.* Fig. 2.3) centered about the trajectory defined by the moveout generated by Eq. (2.4) or Eq. (2.5). From Eq. (2.6) it follows that Semblance expresses the ratio of output/input energy within the selected window.

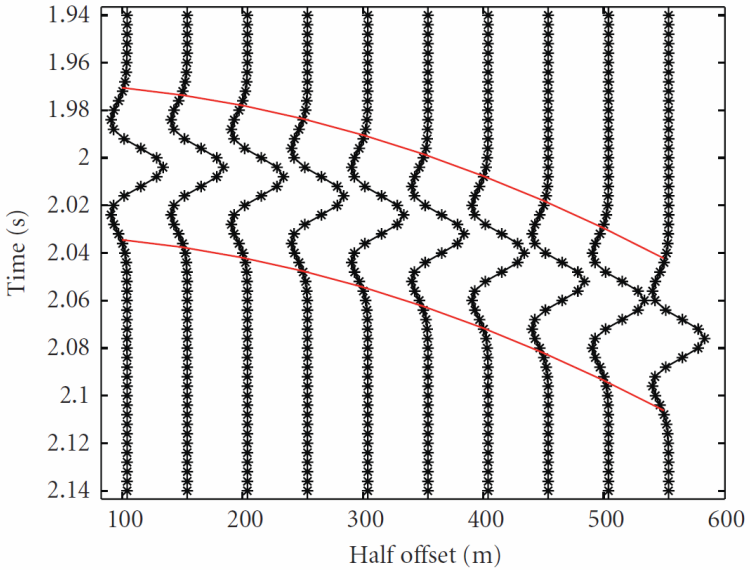

Fig. 2.3. *Time window used to evaluate Semblance defined by red curves (Asgedom et al., 2011 c).*

Chapter 3 GENERATION OF TEST DATA

In this chapter we will generate a simple synthetic data set to be used to test out the CRS-based diffraction separation technique. The model consists of a horizontal reflector and a nearby scatterer embedded in a homogeneous background. Since the separation technique is based on traveltimes (i.e. kinematics) we do not model amplitude effects. The acquisition geometry resembles that of marine seismic with a moving source attached a multiple-receiver line (streamer). Figure 3.1 gives an overview of the acquisition geometry and model. The use of these test data as input to the diffraction separation technique will be discussed in Chapter 4.

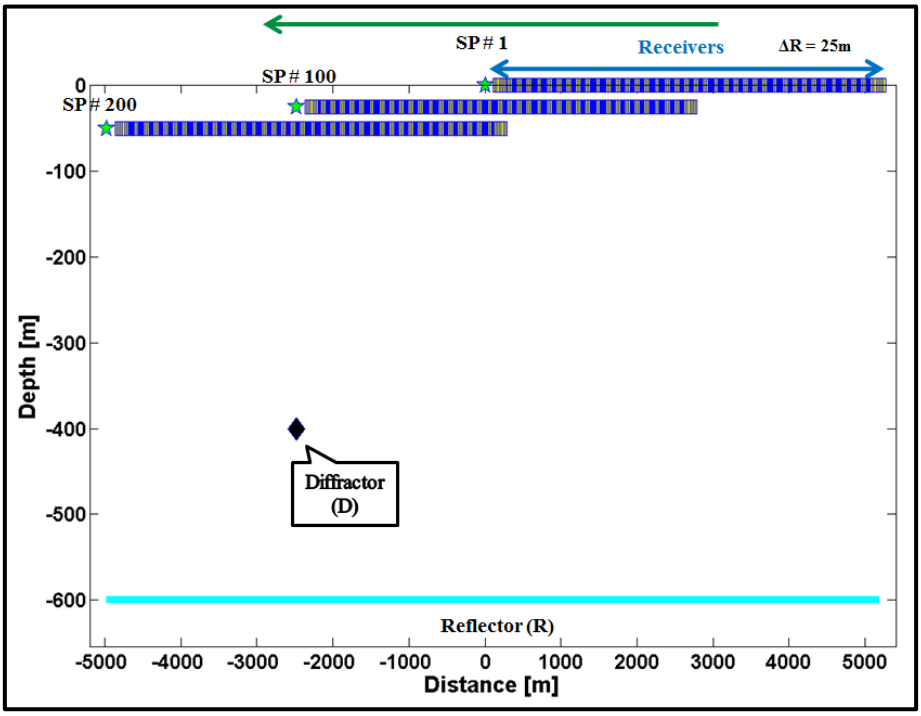

Fig. 3.1. *Acquisition geometry and model. Green arrow indicates the movement of a source with multiple receivers.*

Table. 3.1. *Seismic acquisition parameters.*

No. of sources	**200**
Source interval	25m
No. of receivers	200
Receiver interval	25m
Min. source-receiver offset	200m
Depth of diffractor	400m
Depth of reflector	600m
Velocity above reflector	3000m/s
Central frequency	30Hz

Seismic data have been generated using the set of seismic acquisition parameters shown in Table 3.1. When generating the synthetic data several assumptions were made:

i) The velocity change across the reflector is so weak that no critical events will be generated for this model.

ii) Since only traveltime curves are of key interest we assign a constant reflection coefficient of 1 to every reflected event (neglecting angle dependency, spherical divergency, attenuation and so on).

iii) The diffracted events are assigned a diffraction coefficient of one (same argument as for ii), i.e. travel time curve is the main objective).

The horizontal reflector is placed at a depth of 600m and the diffractor at a depth of 400m. Moreover, the lateral position of the scatterer is given by the coordinate x = -2500m (see Fig.3.1).

3.1 REFLECTIONS

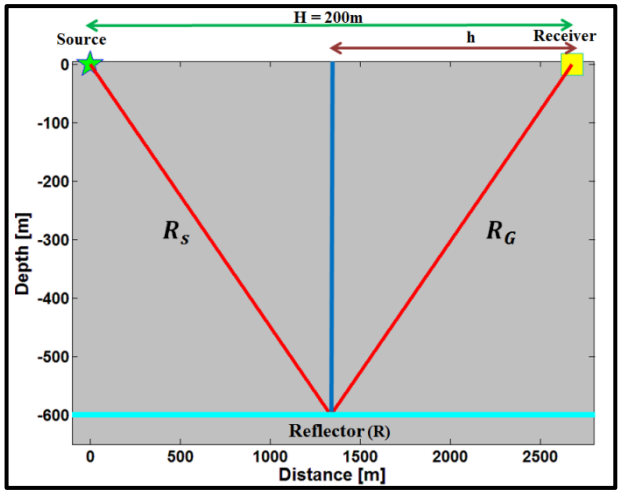

Fig. 3.2. *Traveltime from source to reflector and back to receiver.*

The traveltime equation for reflections associated with a horizontal reflector is (Fig. 3.2)

$$t = \frac{R_S}{v} + \frac{R_G}{v}, \qquad \frac{R_S}{v} = \frac{R_G}{v} = \sqrt{t_o^2 + \frac{H^2}{v^2}} \tag{3.1}$$

where t_0 is the traveltime at zero-offset, $H = 2h$ is the source-receiver offset (h being the half-offset), v is the velocity, R_s is the distance from the source to a specular reflection point and R_G is the distance from the same reflection point to the receiver. Seismic traces were generated using the linear convolution model which reads if noise is included (Eq. 3.2) (Fig. 3.3).

$$x(t) = s(t) * r(t) + n(t) \tag{3.2}$$

where $x(t)$ is the seismic trace, $s(t)$ is the source pulse, $r(t)$ is the reflectivity series and $n(t)$ is the noise (Fig. 3.3). In the simulations, a Ricker wavelet was used with a center frequency of 30 Hz and the noise level was set to zero.

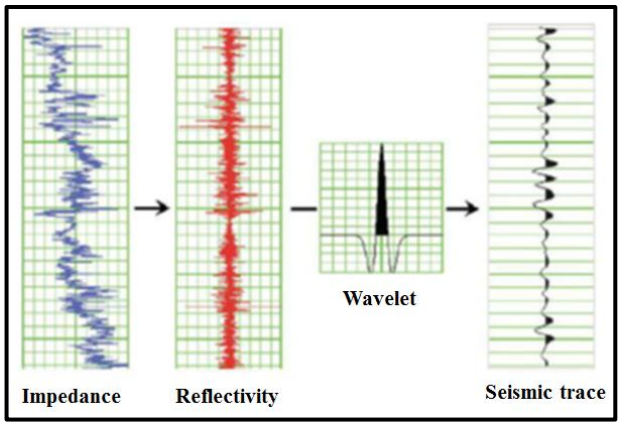

Fig. 3.3. *General convolutional model (after Mondol (2010)).*

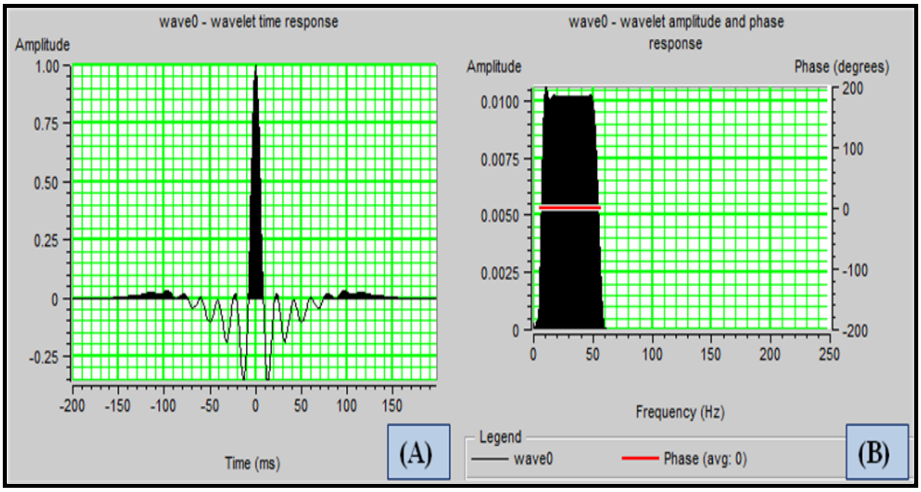

Fig. 3.4. *Ricker wavelet (bandpass linear wavelet, 5/10-50/60, sample rate 2ms, wavelet length= 40) in time domain (A) and frequency domain (B).*

The Ricker wavelet can be expressed as

$$Ricker\ (t) = (\,1 - 2\,\pi^2\,f^2t^2)exp(\,-\pi^2f^2t^2) \tag{3.3}$$

where f is frequency in Hertz, t is time in sec and π is irrational number (Ricker, 1953). Figure 3.4 shows the bandpassed Ricker wavelet used, both in time and frequency domain.

3.2 DIFFRACTIONS

In case of diffractions, the double square root equation is used (Eq. 3.4):

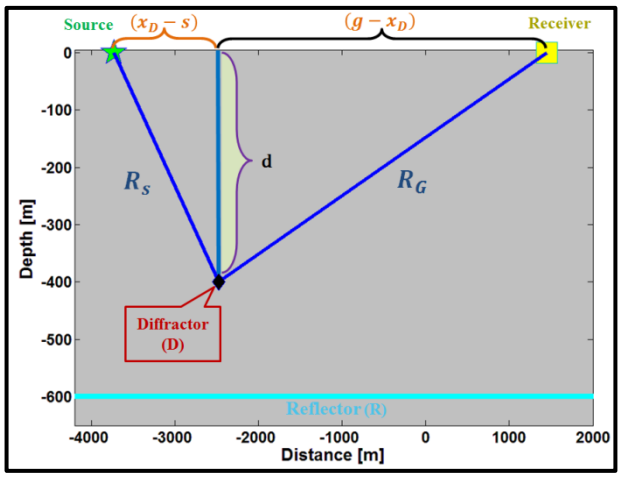

Fig. 3.5. *Traveltime from source to diffractor and back to receiver.*

$$T = T_s + T_G = \frac{R_s}{v} + \frac{R_G}{v} = \sqrt{\frac{(x_D - s)^2 + d^2}{v^2}} + \sqrt{\frac{(g - x_D)^2 + d^2}{v^2}} \tag{3.4}$$

$$R_G = \sqrt{(g - x_D)^2 + d^2},$$

$$R_s = \sqrt{(x_D - s)^2 + d^2}$$

where

T_s = traveltime from a source to the diffractor

T_G = traveltime from the diffractor to a receiver

R_s = distance from a receiver to the diffractor

R_G = distance from a source to the diffractor

s = lateral position of a source

g = lateral position of a receiver

x_D = lateral position of the diffractor

v = velocity

d = depth of the diffractor

Again the same Ricker wavelet was used as a source signal.

3.3. COMMON SHOT GATHER

First we simulate seismic data being acquired in the source-receiver (s, g) domain forming a series of shot gathers. Each source generates data which are recorded at several receivers (Figs. 3.1 and 3.2). Figure 3.6 shows the rays associated with shotpoint (SP) number 200. The corresponding seismic data are shown in Fig. 3.7.

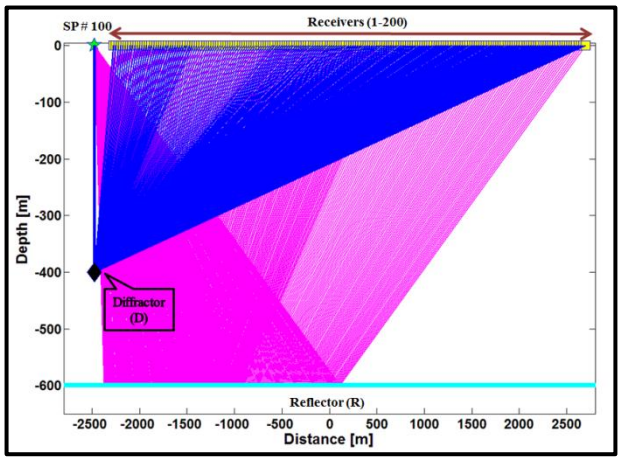

Fig. 3.6. *Rays associated with the diffraction and reflection responses for shotpoint (SP) # 100.*

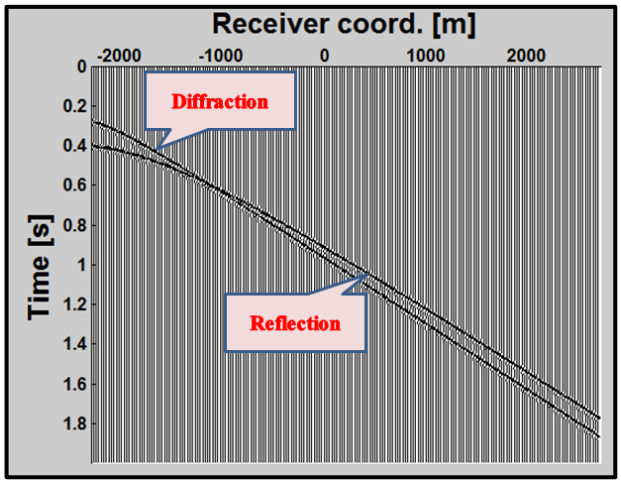

Fig. 3.7. *Reflection and diffraction data for SP # 100.*

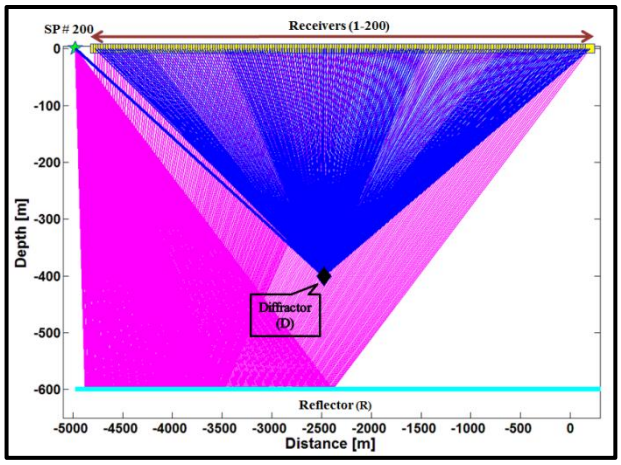

Fig. 3.8. *Ray associated with the diffraction and reflection responses for SP # 200.*

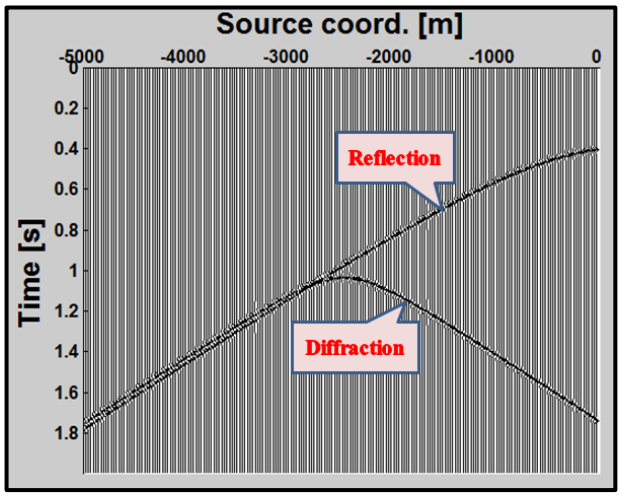

Fig. 3.9. *Reflection and diffraction data for SP # 200.*

Figures 3.8 and 3.9 show the same type of plots, but this time for SP 200 (see Fig. 3.1). Reflections and diffractions look very similar and are more difficult to differentiate for SP 100. This corresponds to the case where the source is placed directly above the diffractor (Fig. 3.5). Moving the source away from the diffractor leads to a better separation between the two events as shown in Fig. 3.9.

3.2. COMMON RECEIVER GATHER

In a common receiver gather the seismic traces represent contributions from the same receiver position. Figure 3.10 shows the rays associated with receiver position 100, and the

corresponding seismic responses are shown in Fig. 3.11. In this case the receiver is almost just above the scatterer. When the receiver moves away (position 200), Figs. 3.12 and 3.13 show that the events now separate well in time.

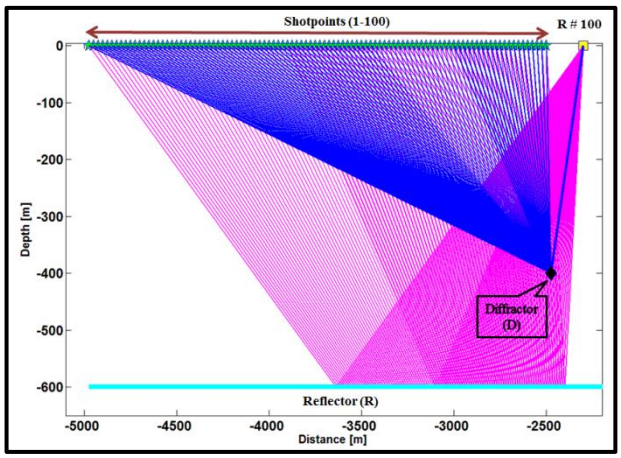

Fig. 3.10. *Common receiver gather ray paths (receiver # 100).*

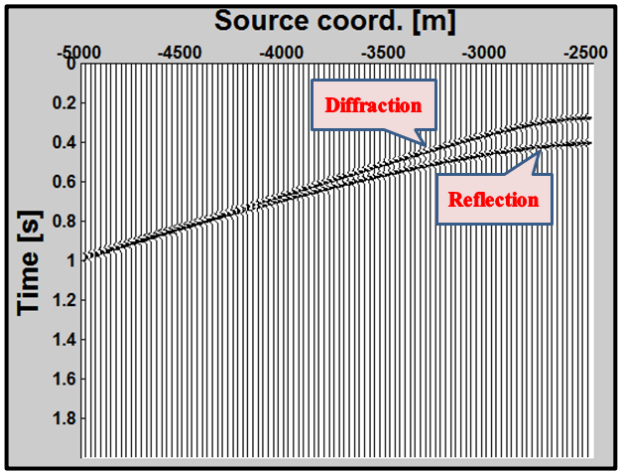

Fig. 3.11. *Common receiver gather reflection and diffraction responses (receiver # 100).*

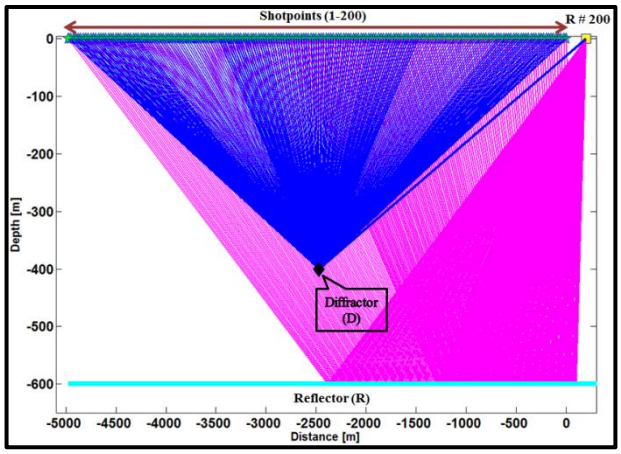

Fig. 3.12. *Common receiver gather ray paths (receiver # 200).*

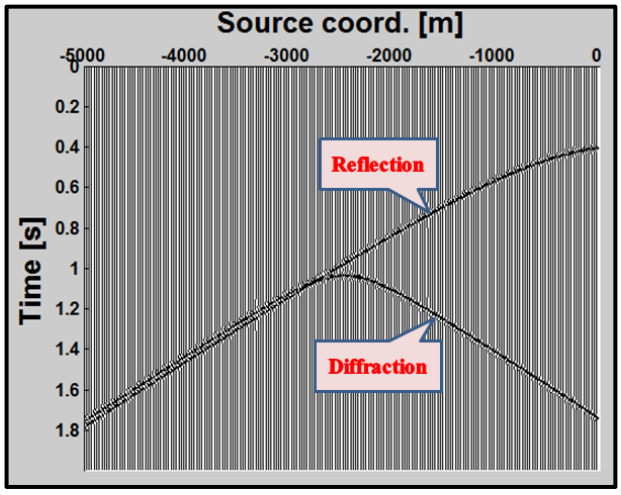

Fig. 3.13. *Common receiver gather reflection and diffraction responses (receiver # 200).*

By comparing Figs. 3.7 and 3.9 with 3.11 and 3.13, it is clear that the common receiver gather is a mirrored version of the common source gather (follow from reciprocity considerations).

3.3. COMMON MIDPOINT GATHER

Seismic processing is traditionally carried out in the midpoint-half-offset (y, h) domain. The midpoint (y) is located midway between a given source-receiver pair. Traces that belong to the same midpoint (y) but with different half-offsets (h) form a CMP gather. Such a gather is also called a CDP (common depth point) gather if we assume a horizontally layered Earth (Fig. 3.14).

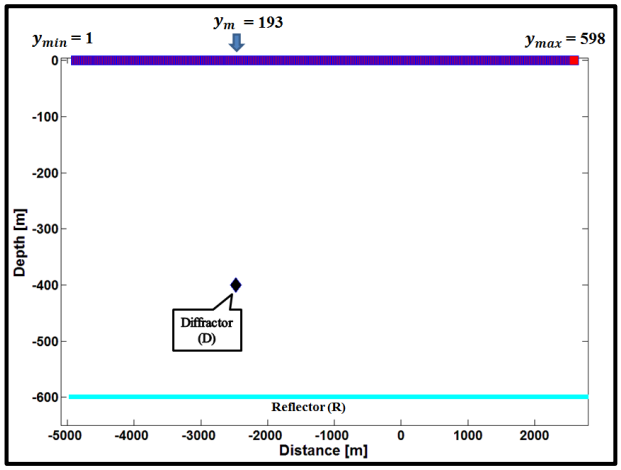

Fig. 3.14. *Midpoint coordinate number ranging from a minimum of 1 (left) to a maximum of 598 (right). Model consists of a diffractor (D) and a reflector (R).*

The coordinate transformation from acquisition domain (source and receiver) to midpoint-offset domain is given as

$$y = \frac{g+s}{2}, h = \frac{g-s}{2} \tag{3.5}$$

where s is the lateral position of a source, g is the lateral position of a receiver, y is the lateral position of the midpoint and h is the half-offset. Figures 3.15 and 3.17 give the rays associated with two different CMP (midpoint) locations, respectively CMP # 100 and CMP # 193.

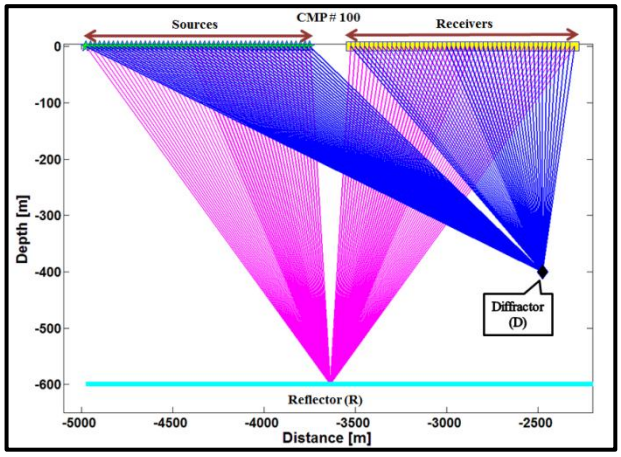

Fig. 3.15. *Ray diagram of common midpoint configuration (CMP # 100).*

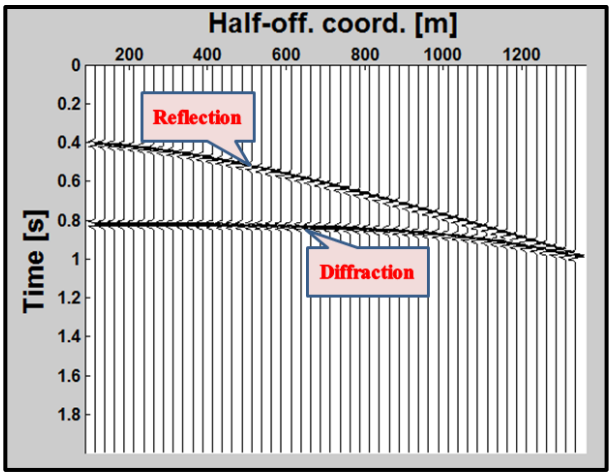

Fig. 3.16. *Common midpoint gather with reflection and diffraction responses (CMP # 100).*

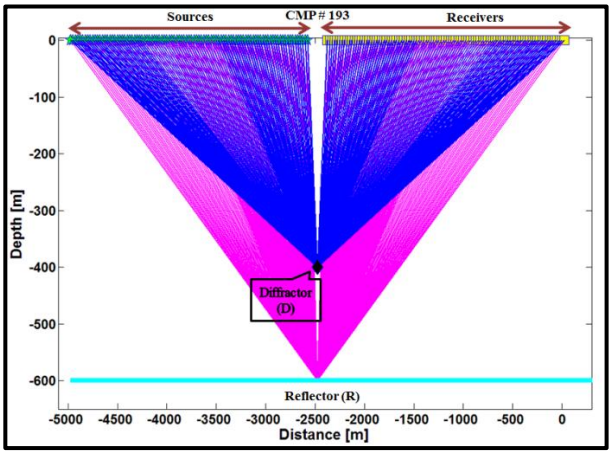

Fig. 3.17. *Ray diagram of common midpoint configuration corresponding to CMP # 193.*

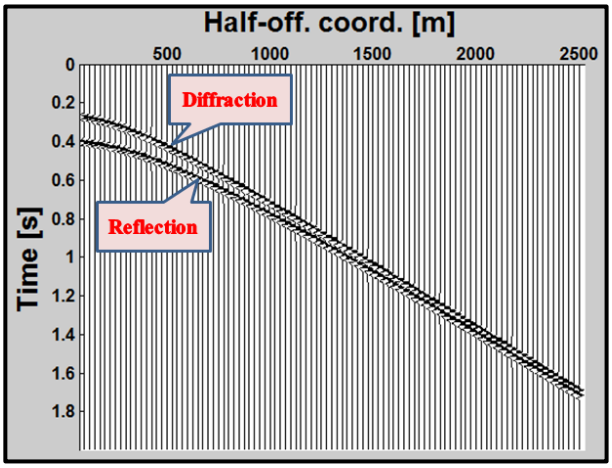

Fig. 3.18. *Common midpoint gather with reflection and diffraction responses (CMP # 193).*

The corresponding seismic responses are shown in Figs. 3.16 and 3.18. The further away the midpoint is from the diffractor, the better separation between the two events. In case the midpoint is located just above the diffraction, the two events fall very close to each other (Fig. 3.18).

3.4. COMMON OFFSET GATHER

A common offset gather contains all traces with a fixed offset selected from all possible source-receiver pairs (Figs. 3.19 and 3.21). Two different offsets are being investigated. Figures 3.19 and 3.20 show respectively the ray diagram and the seismic response in case of a small offset (half-offset # 10 corresponding to a distance of 425 m). Correspondingly, Figs. 3.21 and 3.22 show the same results in case of a large offset (half-offset # 100 corresponding to a distance of 2675 m).

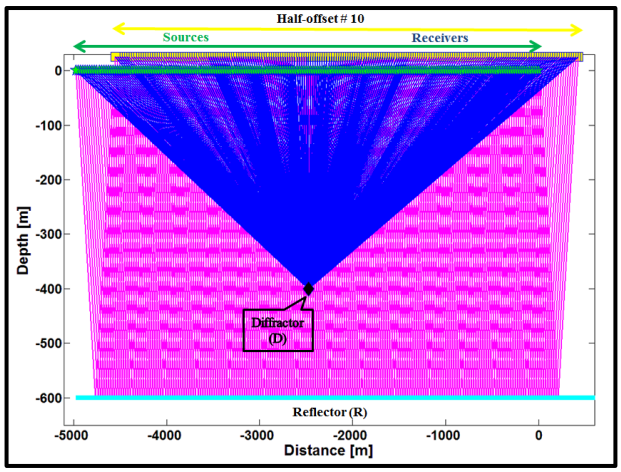

Fig. 3.19. *Ray diagram of common offset configuration (half-offset # 10).*

.

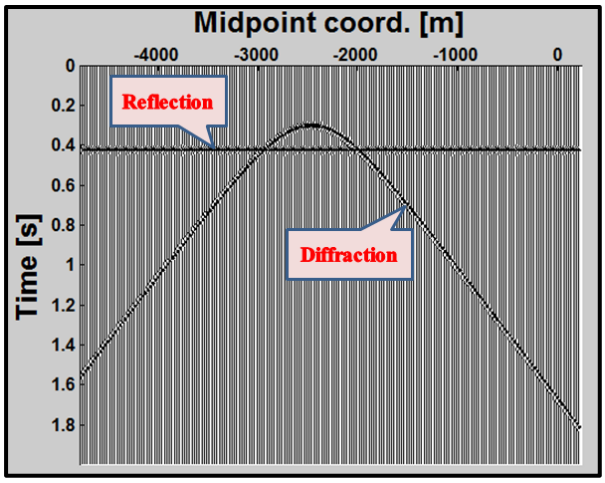

Fig. 3.20. *Common offset gather with reflection and diffraction responses (half-offset # 10).*

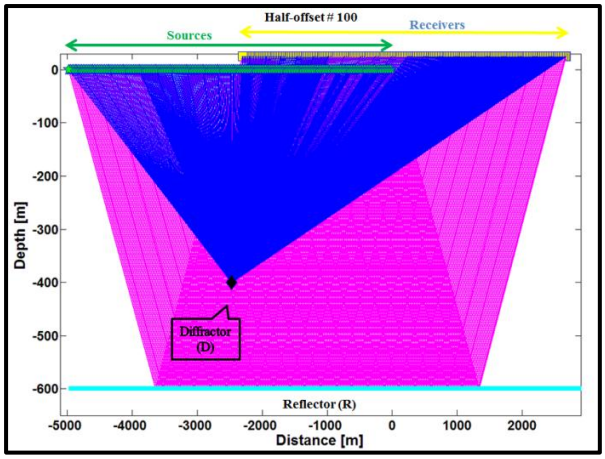

Fig. 3.21. *Ray diagram of common offset configuration (half-offset # 100).*

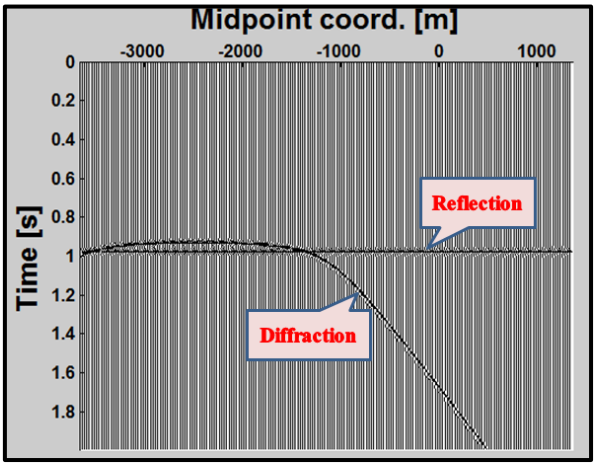

Fig. 3.22. *Common offset gather with reflection and diffraction responses (half-offset # 100).*

For both offset cases the reflection from the horizontal layer appears as a horizontal event. Moreover, the reflection is well separated from the diffraction in both cases. However, by increasing the offset, the apex of the diffraction become more flat (Fig. 3.22).

3.5 SUMMARY OF OBSERVATIONS

Table 3.2 summarizes the main observations made from this simple synthetic study. A good separation is characterized by '+' and the opposite by '-'.

Table 3.2. *Separation of reflection and diffraction in different domains.*

Sorting	Close to diffractor	Far from diffractor
Common source gather	-	+
Common receiver gather	-	+
Common midpoint gather	-	+
Common offset gather	+	+

According to Table 3.2 all different domains discriminate well between reflections and diffractions in case the diffractor is displaced to the sides. Note that in practice, however, this will not always be true. If the nearby reflection is dipping the result may be different. Also, that part of the diffraction response being more linear is characterized by smaller amplitude and thus more vulnerable to noise.

In this thesis diffraction separation will be carried out in a two-step procedure, involving both data sorting in CMP gather as well as ZO-stacking. The latter sorting is similar to the CO sorting discussed here in case of the small offset.

Chapter 4 DIFFRACTION SEPARATION BASED ON CRS-TECHNIQUE

In this chapter the performance of the CRS-technique is being tested using the controlled data from the previous chapter. To make the test data more realistic, white Gaussian noise with 5% variance was included.

During this CRS-analysis several assumptions were made:

i) Small offset is used for the stacking and velocity analysis.

ii) Data are multiple free.

iii) Only pressure (P) waves were considered.

iv) Since no direct and refracted waves were taken into account and streamer is placed at datum (0m), both muting and static corrections could be skipped.

v) Automatic gain control (AGC) is not applied since we are neglecting amplitude losses (geometrical spreading, intrinsic attenuation and transmission losses).

vi) Since the reflector and diffractor are located at shallow depths therefore NMO-stretch is not negligible (Gelius and Johansen, 2010).

vii) In general, energy of the diffractions are much weaker than that of reflections (Fomel et al., 2007). However, in this simple study their amplitude levels are set equal on purpose in order to understand better the technique.

4.1 MAIN STEPS FOR CRS ANALYSIS

Separation of diffractions from reflections employing the CRS-technique can be divided into two main steps:

i) A CMP velocity analysis has to be carried out corresponding to the condition $\Delta m = 0$ in Eq. (2.3) to find the value of the parameter $C = \frac{4}{V_{rms}{}^2}$, where V_{rms} is the root mean square velocity considered to be the stacking velocity in case of small offsets.

ii) After step i), the data are stacked to form an approximate zero-offset (ZO) section. Then the parameter A can be determined from Eq. (2.3) by setting $h = 0$.

Data are now stacked along the traveltime curve given by Eq. (2.3) for various values of A, and within a user defined aperture (related to the Fresnel zone). To identify optimal parameter values for both A and C a coherency measure needs to be applied. Here we use Semblance (*cf.* section 2.5) with a window size of 13 samples. Finally, a diffraction stacked section is then generated using Eq (2.3) once more with the optimal parameter sets.

4.2 CMP DOMAIN ANALYSIS

In this section we will give examples from the velocity analysis to obtain further insight about the CRS-technique. More specifically, we will consider two CMP locations, i.e. # 100 and 193 (*cf.* Figs. 3.15 and 3.17). In the first case, the apex of the diffractor is displaced from the midpoint location m_o of the central ray. This is schematically shown in Fig. 4.1.

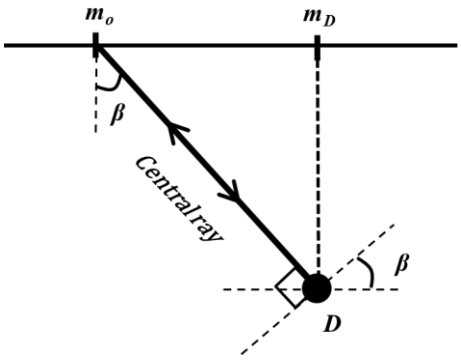

Fig. 4.1. *Displaced diffractor (D).*

Based on this simple analysis it follows that the diffraction response can be interpreted as close to the response from a dipping reflector (dip angle β, see Fig. 4.1). For the simple case of a homogenous background the true velocity v will be modified as $\frac{v}{\cos\beta}$ (Gibson et al., 1983). This implies that when carrying out a velocity analysis on CMP # 100, one should expect that the reflected event will stack at the true velocity of 3000 m/sec but the diffraction response will stack at a much higher velocity. Figure 4.2 shows the velocity spectrum based on Semblance as a coherency measure. This spectrum confirms our expectations regarding the velocities. It also follows directly from Fig. 4.3 which shows the Semblance curve and the corresponding peak velocities. In this velocity analysis the first 1/3 of the full offset range was used (maximum offset of 800m), and velocities were automatically scanned between 1000 and 5000 m/sec. Also a coherency threshold of 0.3 was used.

The results obtained for CMP # 100 supports our earlier observations that if the scatterer is displaced (relative m_o), reflections and diffractions will separate with different C-parameter values. However in many practical cases, diffractions will be weaker than reflections. This means that the parameter C will be reflection driven. Thus, the case of a displaced scatterer will be difficult to enhance unless the parameter C is allowed to vary within a range.

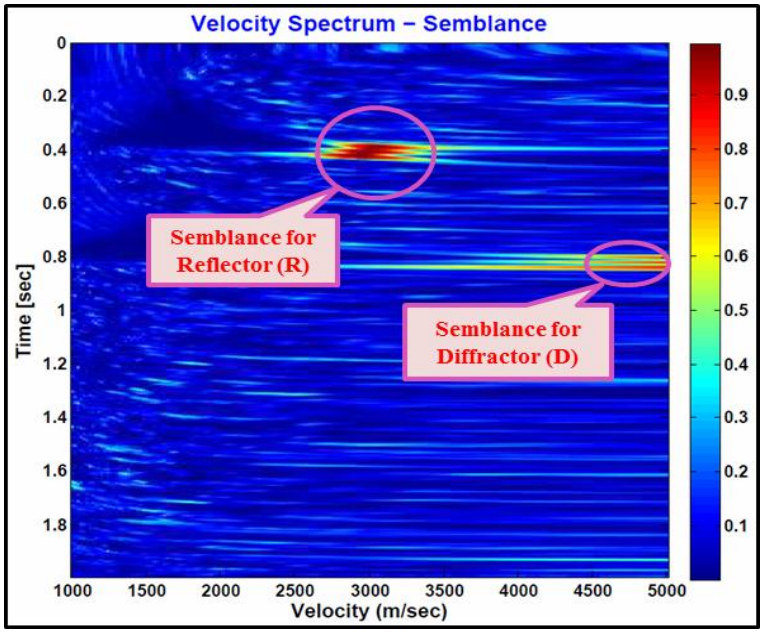

Fig. 4.2. *The coherency map (velocity spectrum) based on Semblance for CMP # 100.*

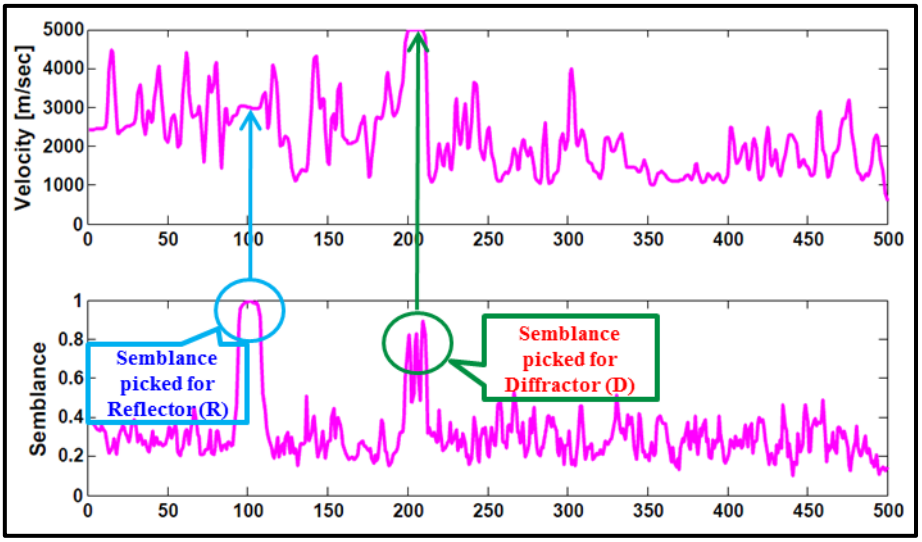

Fig. 4.3. *Semblance peaks picked for reflection (blue circle) and diffraction (green circle), and their corresponding velocities for CMP # 100.*

By using the estimated velocities from Fig. 4.3 a stacked trace can be formed as shown in Fig. 4.4 (after proper muting of NMO stretch).

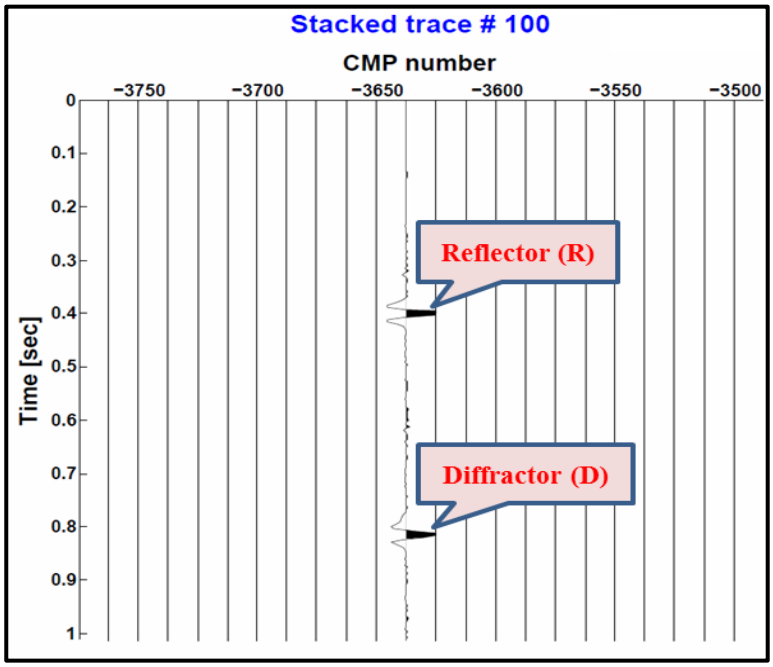

Fig. 4.4. *Stacked trace corresponding to CMP # 100.*

Next, we present the results obtained from the velocity analysis in case of CMP # 193. Now the apex of the diffractor falls directly below the midpoint location m_o of the central ray. Thus, in this case we expect that both the reflection and the diffraction stack optimally at the true medium velocity of 3000 m/sec. This is confirmed by Figs. 4.5 and 4.6. Finally, Fig. 4.7 gives the stacked trace.

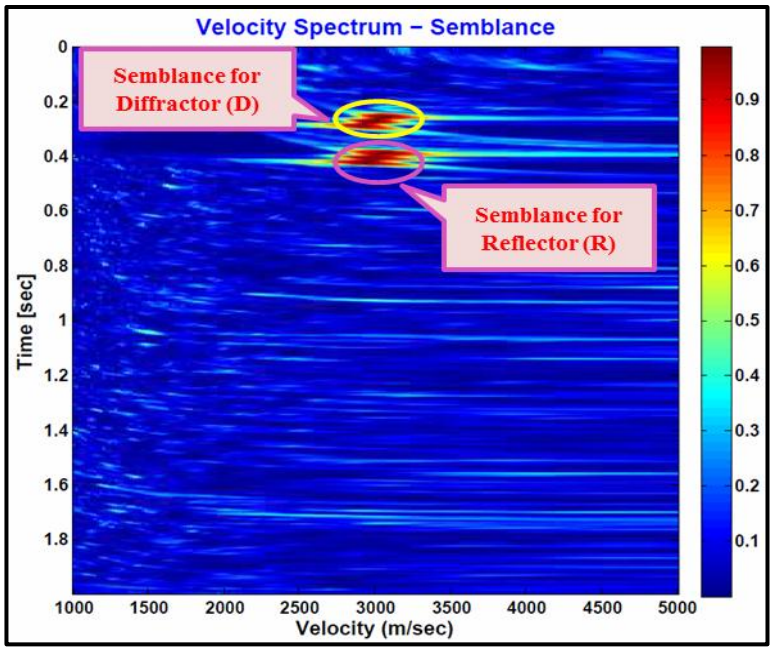

Fig. 4.5. *The coherency map (velocity spectrum) based on Semblance for CMP # 193.*

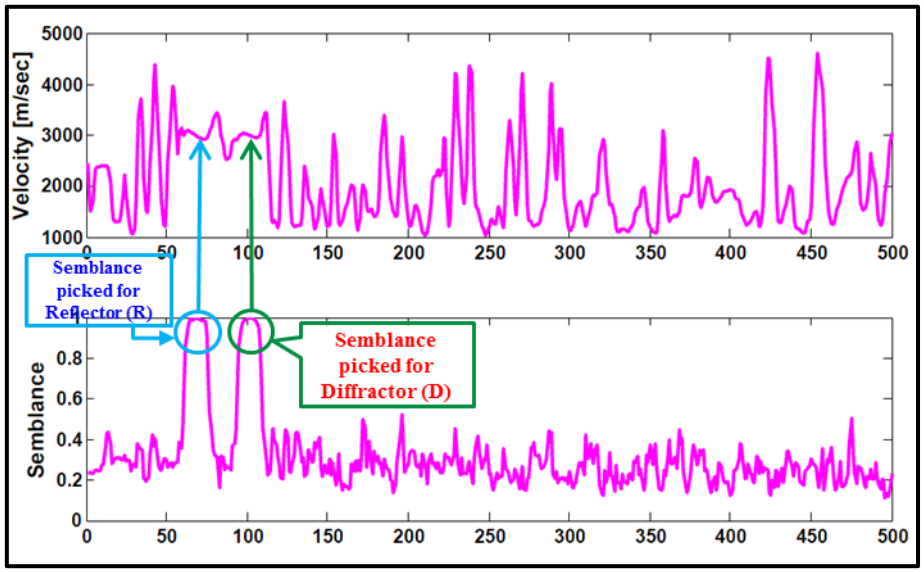

Fig. 4.6. *Semblance peaks picked for reflection (blue circle) and diffraction (green circle, and their corresponding velocities for CMP # 193.*

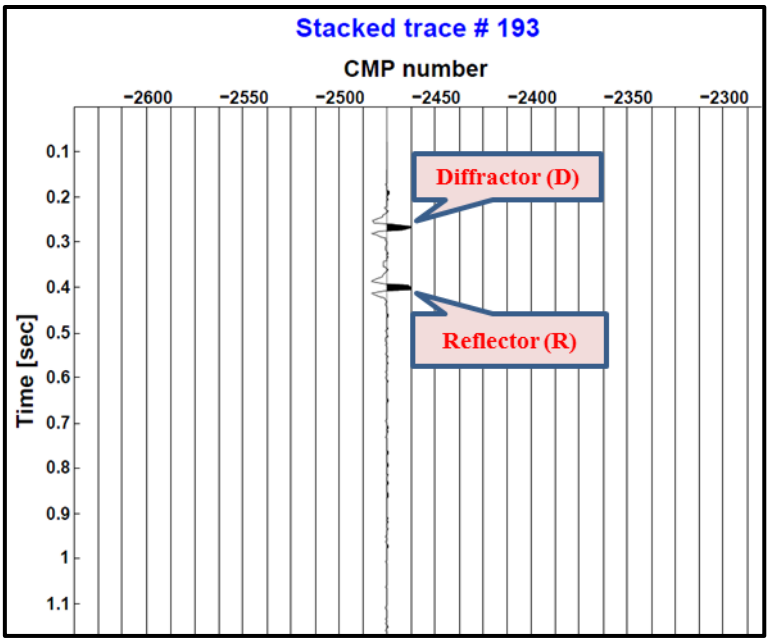

Fig. 4.7. *Stacked trace corresponding to CMP # 193.*

After having completed the velocity analysis for all CMP's, the results can be combined in the two main plots shown in Figs. 4.8 a and b. It follows from the coherency map that high values are associated with the reflection and that part of the diffraction close to the apex. These regions of high coherency also correspond to the correct medium velocity of 3000 m/sec (*cf.* Fig 4.8b).

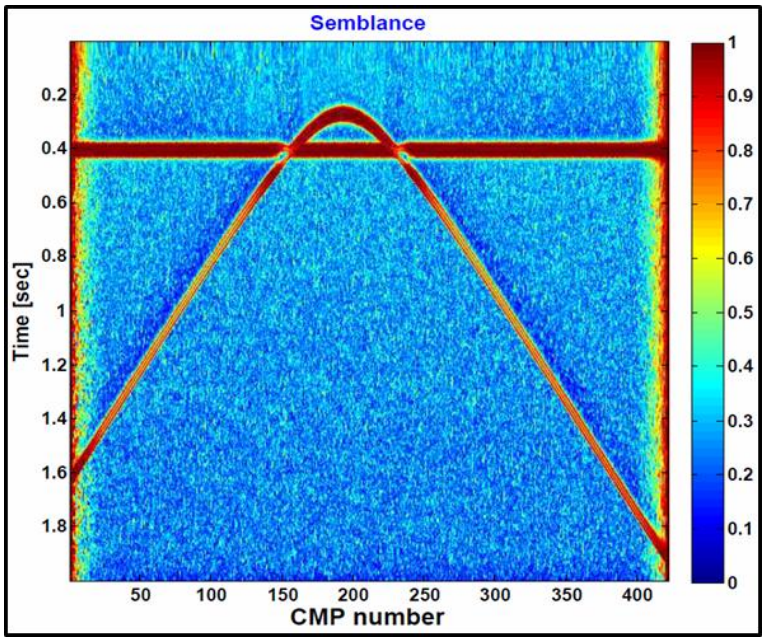

(a)

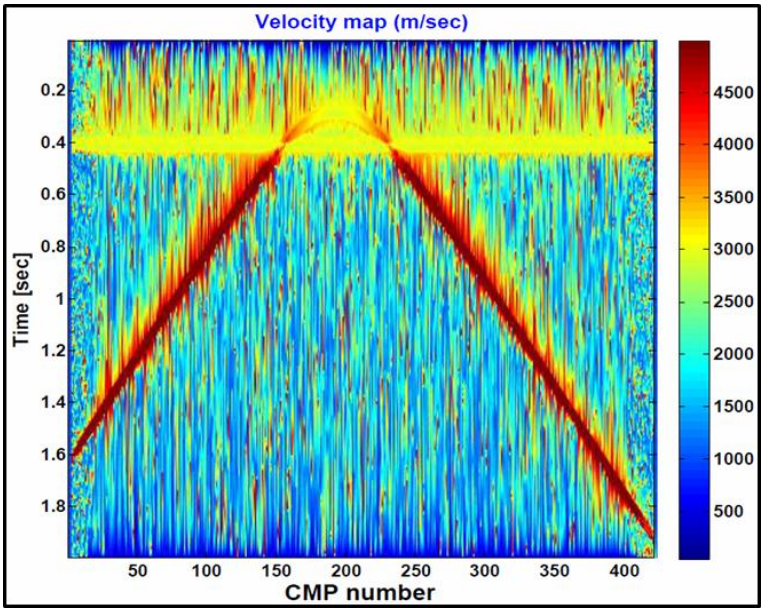

(b)

Fig. 4.8. *The coherency map of parameter C based on Semblance (a) and corresponding velocities in m/sec (b).*

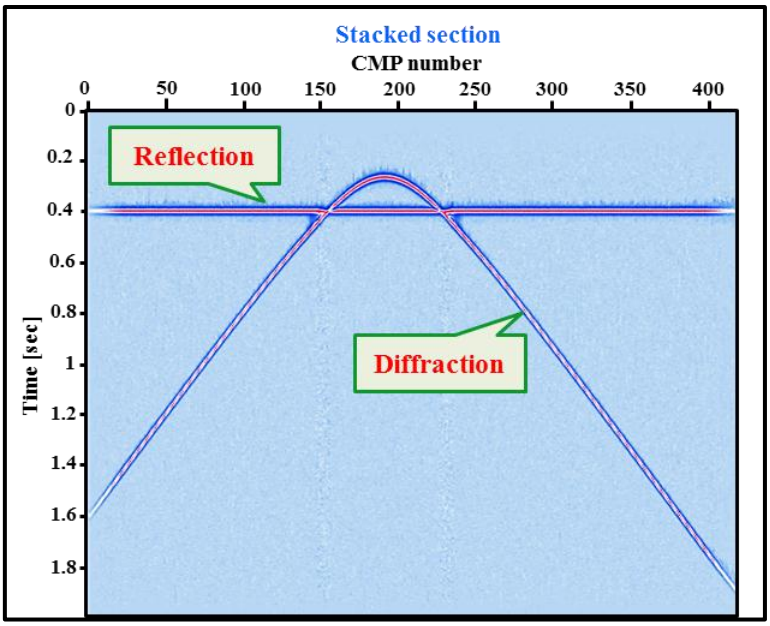

Fig. 4.9. *Stacked section (ZO approximation).*

Finally, the stacked section is shown in Fig. 4.9. This section is assumed to be a good approximation to a ZO section.

4.5 ZO-SECTION ANALYSIS

The second step of the diffraction separation technique can now be carried out. The main emphasis is to estimate optimal values for the CRS parameter A given the values already obtained for the parameter C. If we assume a constant-velocity (v_o) Earth model, we have that $k_{NIP} = \frac{1}{R} = \frac{2}{t_o v_o}$ (Fig. 4.10).

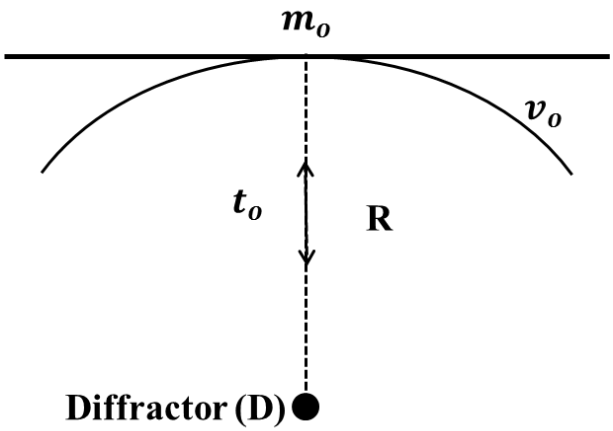

Fig. 4.10. *Illustration diagram of* $\boldsymbol{k_{NIP} = \frac{1}{R}}$ *for a point diffractor (D).*

From Eq. (2.2b) it then follows that

$$C = \frac{2\, t_o cos^2\beta k_{NIP}}{v_0} = \frac{4cos^2\beta}{v_0^2} =$$

$$\frac{4}{v_0^2}(1 - sin^2\beta) = \frac{4}{v_0^2}\left[1 - \left(\frac{Av_0}{2}\right)^2\right] \tag{4.1}$$

For the simple case of a homogenous background, knowing parameter C gives directly the corresponding value of parameter A using Eq. (4.1). However, errors in the C parameter estimates will propagate to the corresponding A values using this approach.

Since Eq. (4.1) represents a 1D parametric search (through the link between A and C) a more refined parametric analysis can be carried out. The full theoretical range of β-values will be between the values $\pm\frac{2}{v_o}$ (*cf.* Fig. 4.12). The aperture size was set to 2 times the Fresnel zone. By discretizing A in 101 values between these bound and search for the optimal ones (and with the corresponding C value given by Eq. (4.1)), the coherency map shown in Fig. 4.11a is

obtained. It can be seen that the whole diffraction is characterized by a high Semblance value. Figure 4.11b shows the corresponding apparent velocity values calculated from parameter C. As expected, only close to apex the velocities resemble the true medium velocity. From Eq. (2.2b) it follows that the emergence angle β can be computed from the parameter A, i.e. $\beta = \arcsin\left(\frac{Av_0}{2}\right)$. Figure 4.12 shows a plot of β for this example. Large values of β correspond to high apparent velocities in Fig. 4.11 b. Finally, based on the optimal sets of parameters A and C, a ZO diffraction-only stack can be generated as shown in Fig. 4.13. It can be easily seen that the CRS based diffraction separation technique has worked well in this simple case.

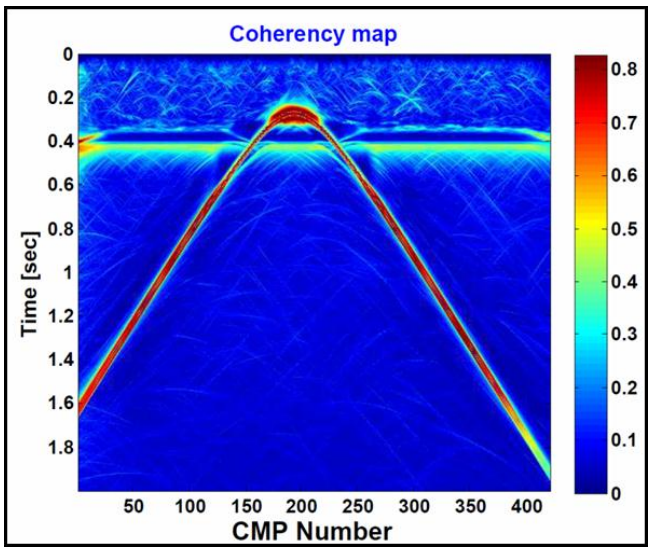

(a)

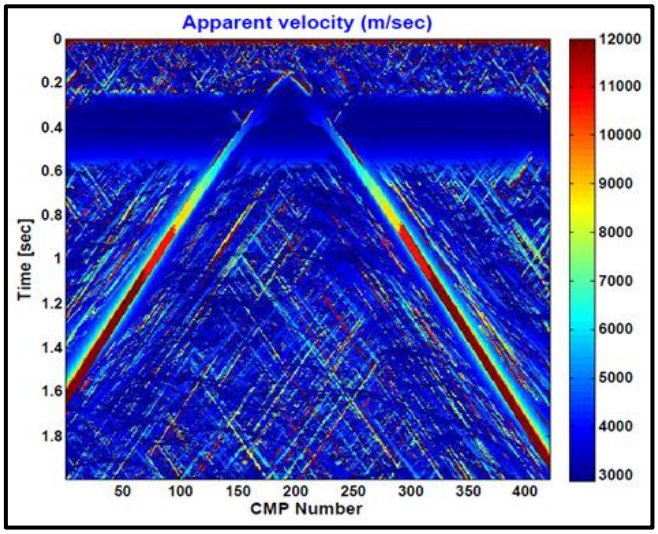

(b)

Fig. 4.11. *The coherency map of parameter A based on Semblance (a) and corresponding apparent velocities (b).*

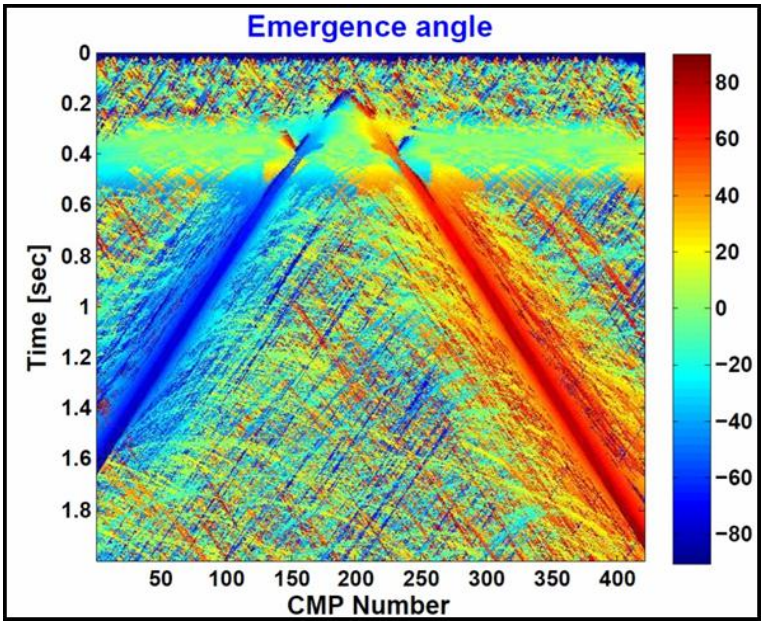

Fig. 4.12. *Range of emergence angles (β) estimated from parameter A.*

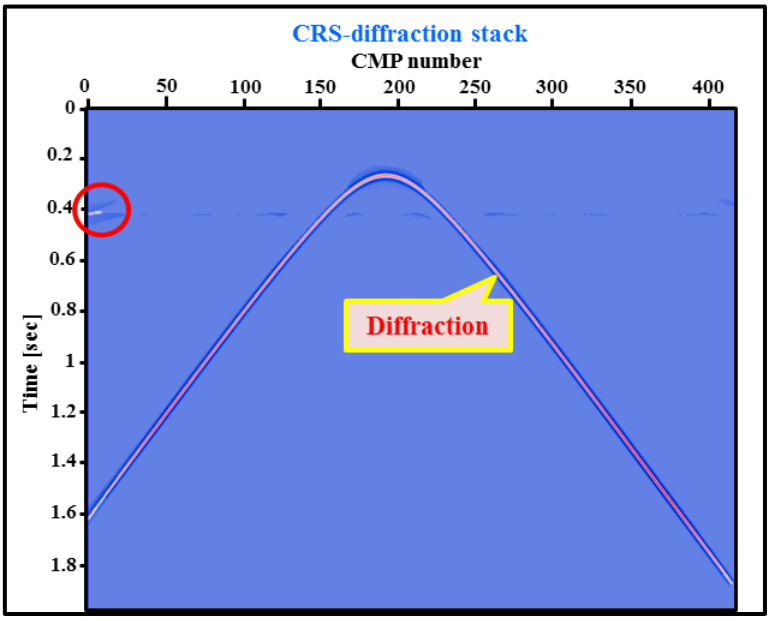

Fig. 4.13. *A zero-offset CRS-diffraction stack based on optimal sets of parameters A and C. Red circle indicates edge effects.*

4.6 DIFFRACTION IMAGING BY APEX DETECTION

A ZO diffraction-stack like the one shown in Fig. 4.13 can be further migrated to obtain an image of the scattering structures. Alternatively, the location of a scatterer can be estimated employing apex detection. Assume that the scatterer is located vertically below the midpoint coordinate m_o of the central ray. In this case it follows directly from Eq. (2.2b) that the CRS-parameter $A = 0$. Thus, since the values of parameter C are already known, we can use Eq. (2.5) (setting $A = 0$) to generate apex locations by stacking within the conventional ZO stack. If the stacking response is represented by a coherency measure like Semblance, an apex 'image' like the one shown in Fig. 4.14a can be obtained. The true apex location is characterized by the highest coherency, but also some contributions associated with the reflector can be seen. This can be due to inaccuracies in the C-parameter and also that we only employed the first 1/3 of the full offset range when forming the conventional ZO stack. Finally, by introducing a coherency threshold of 0.3 in Fig. 4.14a and setting all values above to one and the rest to zero the binary map shown in Fig. 4.14b is obtained. We denote this image an apex detection map. We can now see that only one scatterer is identified as it should, and also that the location is the correct one.

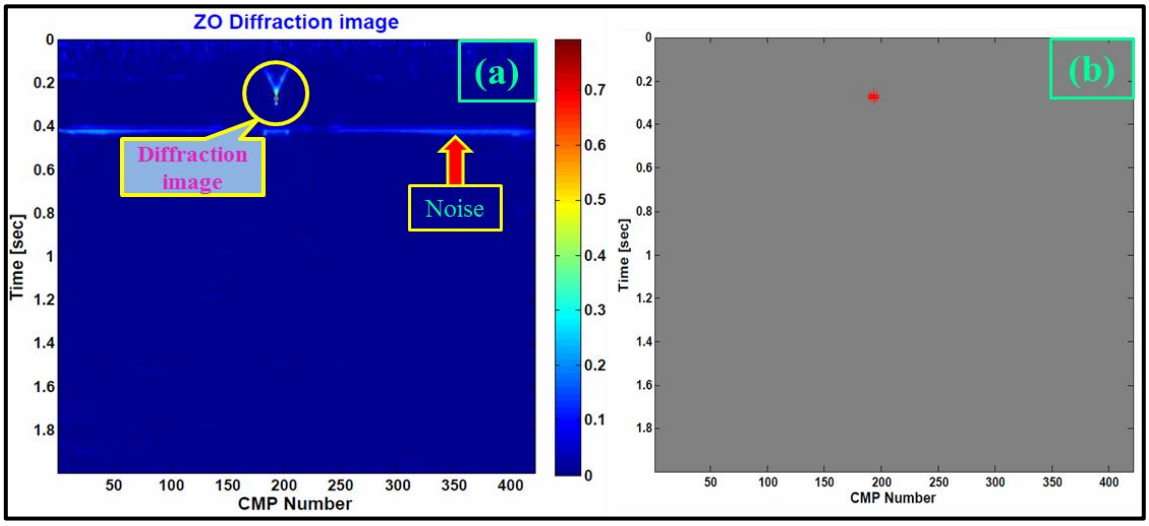

Fig. 4.14. *Apex coherency image (a) and apex detection map (binary type) obtained after coherency thresholding(b).*

Chapter 5 SIGSBEE2A DATA EXAMPLE

In this Chapter, the post-stack diffraction separation method is applied to the complex 2D synthetic dataset named Sigsbee2a generated by SMAAT JV (Paffenholz, 2001). In this dataset the velocity-depth model is analogue to the geological settings present in the Sigsbee escarpment in the deep water Gulf of Mexico. The salt body is associated with rough edges. Our main focus will be on those edges since they are likely to generate diffracted energy.
Table 5.1 shows the acquisition parameters used to generate the Sigsbee2a dataset.

Table 5.1. *Acquisition geometry for Sigsbee2a dataset* (*www.reproducibility.org/data/sigsbee/).*

No. of sources	500
Source interval	150ft
No. of receivers	348
Receiver interval	75ft
Min. source-receiver offset	0ft
No. of CDPs	2053
CMP interval	37.5ft
Max. number of traces in CMP gather	87
Central frequency	20Hz
CMP range	500-2000
Maximum depth to image	31000ft
Background Sediment Velocity	5000ft/sec

In this study only a selected part of the Sigsbee2a model was employed, as shown in Fig. 5.1.

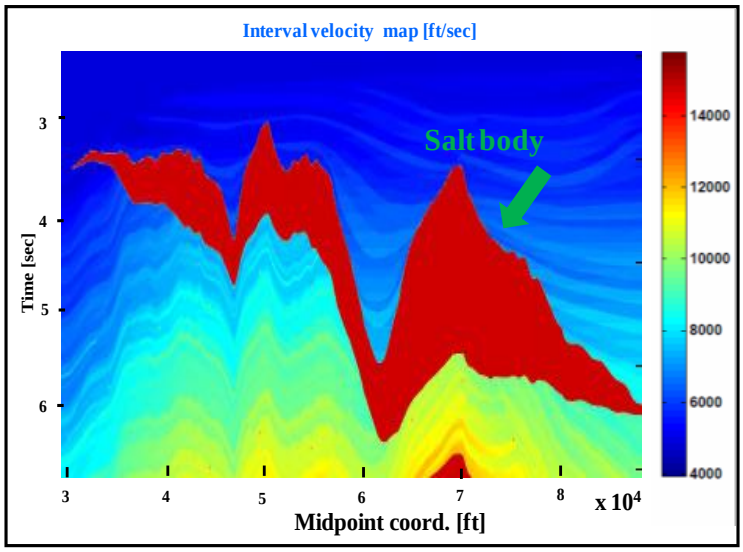

Fig. 5.1. *The selected part of Sigsbee2A model showing the interval velocities (ft/sec) in time.*

NMO velocities were obtained by converting the stratigraphic interval velocities in depth into RMS velocities in time (Asgedom et al., 2012). The latter velocities were assumed to approximate the NMO velocities within the small spread assumption (small offset range). Using these NMO velocities and small aperture a ZO-stacked section has been generated (*cf.* Fig. 5.2). From Fig. 5.2 it follows that both reflected and diffracted energy are clearly visible.

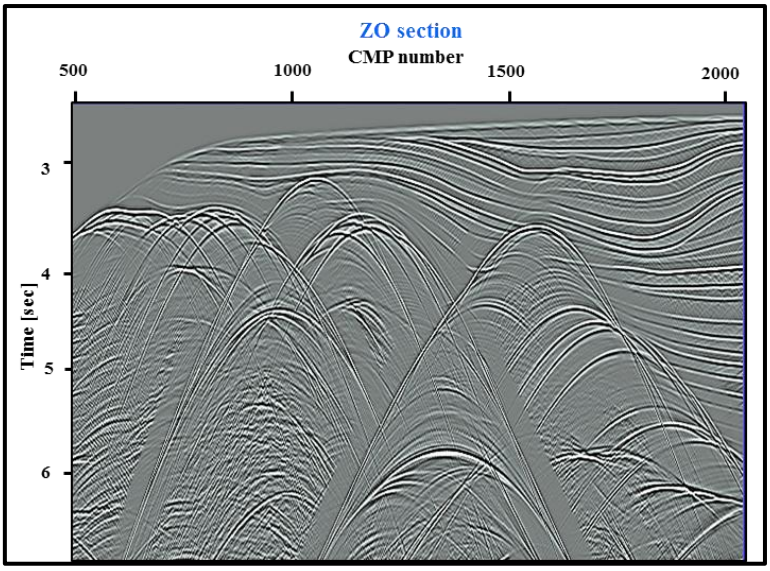

Fig.5.2. *ZO section corresponding to the selected part of Sigsbee2a shown in Fig. 5.1.*

5.1 POST-STACK DIFFRACTION SEPARATION

In case of a homogenous model a simple parametric equation linking the CRS parameters A and C was introduced in section 4.5 (see Eq. (4.1)).

If we assume a horizontally layered Earth model so that the NMO-velocity concept is valid, Eq. (4.1) can be generalized as

$$C = \frac{4}{v_{NMO}^2}\left[1 - \left(\frac{A\, v_{NMO}}{2}\right)^2\right] \tag{5.1}$$

Thus, the stratigraphic medium has been replaced by an effective NMO-medium (straight rays). In general, reflectors will tend to dip within areas of the subsurface. For such cases, the corresponding NMO velocities will be biased and should be compensated by multiplying with the Levin factor cosϕ (Levin, 1971), where ϕ is the dipping angle.

Consequently, in Eq. (5.1) we replace v_{NMO} by $v_{NMO}.cos\phi$:

$$C = \frac{4}{(v_{NMO}\,.\,cos\phi)^2}\left[1 - \left(\frac{A\, v_{NMO}\,.\,cos\phi}{2}\right)^2\right] \tag{5.2}$$

Equation (5.2) can now be used to determine optimal values for the CRS-parameters A and C. Instead of varying directly parameter A we scan over the emergence angle β. Thus, we rewrite Eq. (5.2) as follows:

$$C = \frac{4}{(v_{NMO}.cos\phi)^2}\,[1 - sin^2\beta]\,,\; A = \frac{2sin\beta}{v_{NMO}\,.cos\phi} \tag{5.3}$$

In the parametric analysis we let β vary between $-60^o\ to\ 60^o$ (increment of 1^o), and the dip angle ϕ was set to vary between $0^o\ and\ 60^o$ (increment of 5^o). The aperture size was set to 2.5 times the approximate Fresnel zone. Figure 5.3a shows the coherency map of parameter A based on Semblance, whereas Fig. 5.3b shows the corresponding emergence angles (β) calculated from A. In Fig. 5.3c the apparent velocities derived from the corresponding optimal values of C ($v_{app} = \frac{2}{\sqrt{C}}$) are shown. Finally, Fig. 5.4 shows the ZO CRS-diffraction stack obtained based on the optimal sets of parameters A and C. On comparison with Fig. 5.2, we can see that the diffractions have been efficiently enhanced relative the reflections.

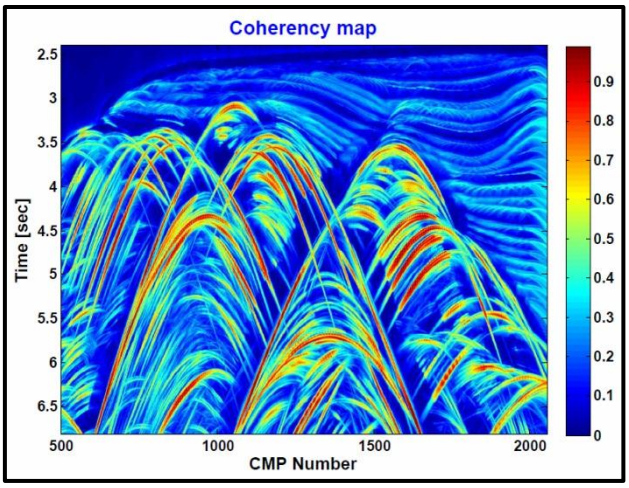

(a)

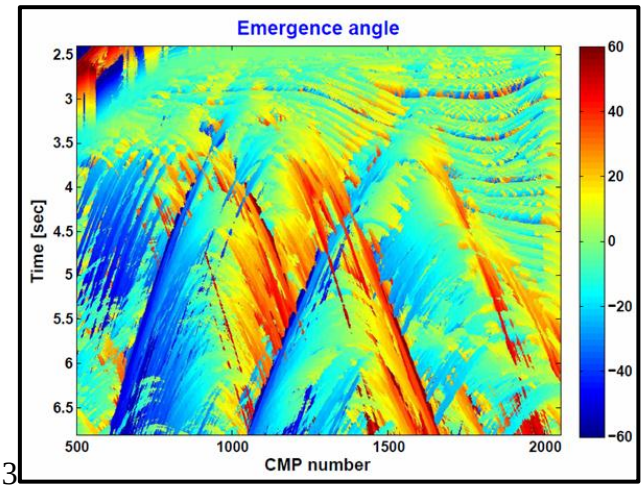

3

(b)

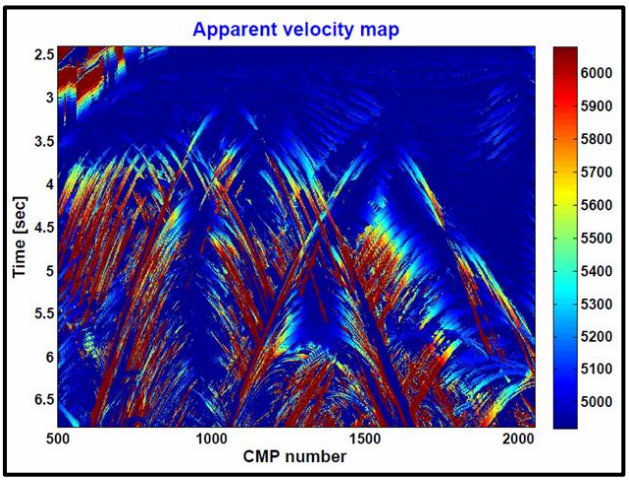

(c)

Fig.5.3. *The coherency map of parameter A based on Semblance (a), the corresponding emergence angles calculated from A (b) and apparent velocities derived from the corresponding optimal values of C (c).*

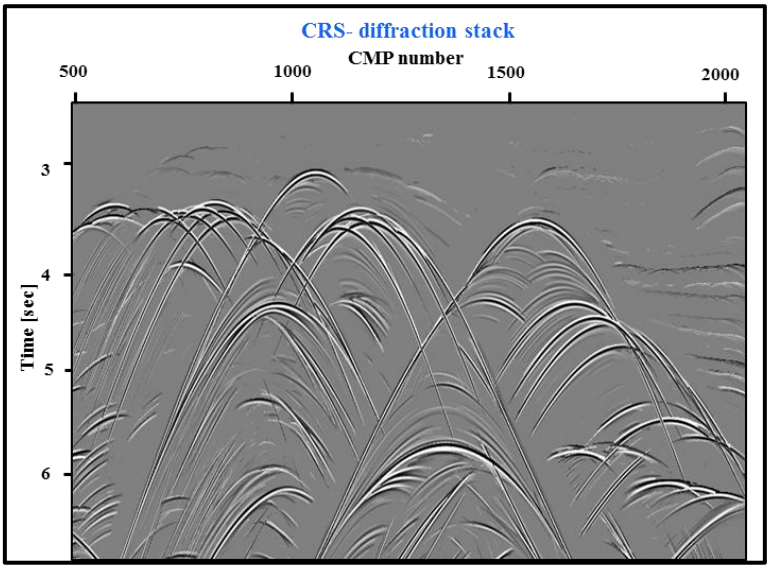

Fig. 5.4. *A zero-offset CRS-diffractions stack based on optimal sets of parameters A and B.*

5.2 DIFFRACTION IMAGING BY APEX DETECTION

By analogy with section 4.6, apex detection type of imaging was also applied to the Sigsbee2a data. The main idea is the same: parameter A is set to zero and by using the already known C values stacking within the conventional ZO section is carried out to generate an apex coherency image as shown in Fig. 5.5a. By using a coherency thresholding of 0.3 the apex detection map (binary type) shown in Fig. 5.5b is finally obtained. The boundary of the salt body has been superimposed the figure and correlates well with the detected apexes. Some parts of the reflectors can also be seen in this map. The reason for this is that the Sigsbee2a data have been generated using finite-difference techniques. This implies that the gridding effect associated with a reflector is interpreted by the separation method as a series of diffractions.

Finally, Fig. 5.6 gives a flow chart showing the main steps associated with respectively forming a diffraction-only stack and a binary apex detection map.

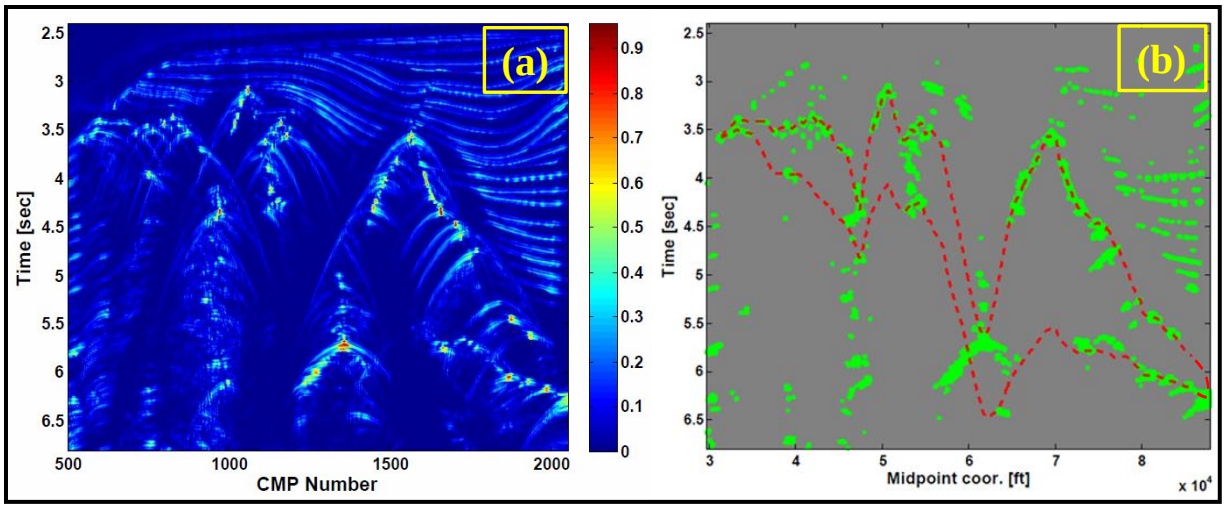

Fig. 5.5. *Apex coherency image (a) and corresponding apex detection map obtained after coherency thresholding (b).*

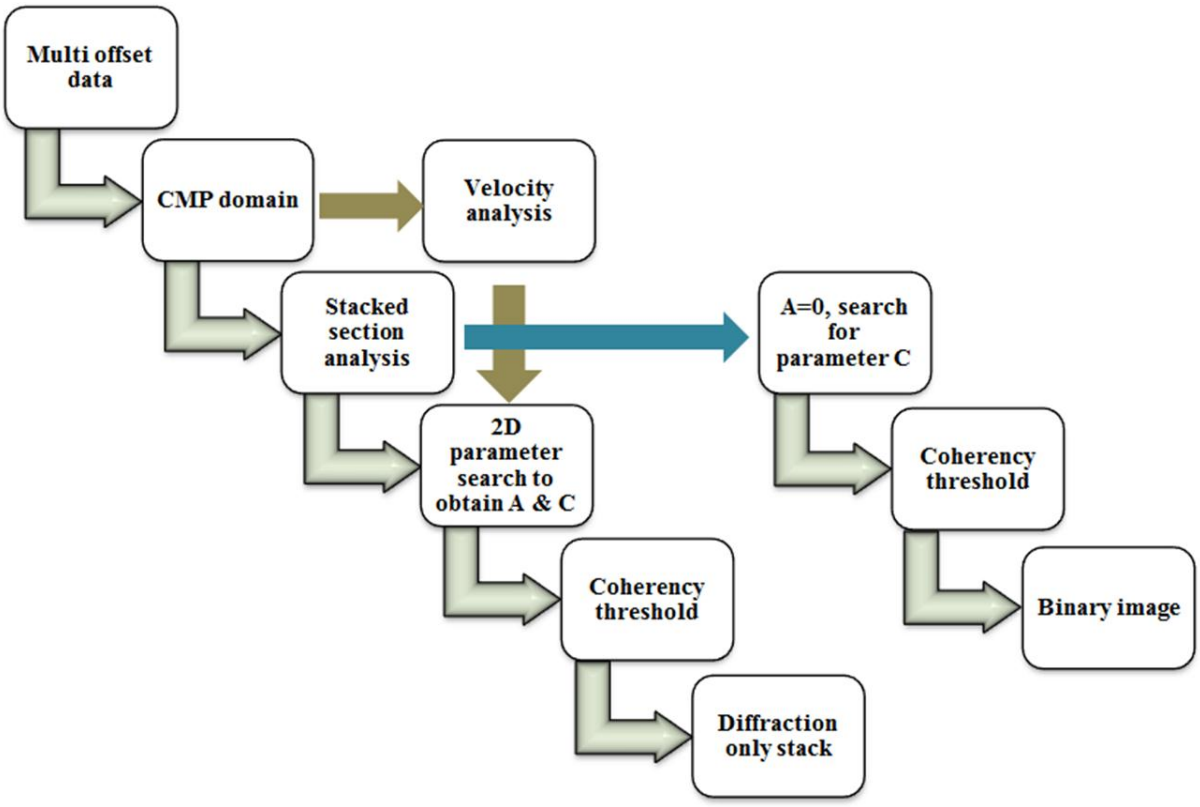

Fig. 5.6. *Flow chart of the main steps that have been followed during the CRS-analysis of the Sigsbee2a dataset.*

Chapter 6 DISCUSSION AND CONCLUSION

In this thesis the feasibility of using the modified CRS-technique to separate diffractions from reflections has been investigated. This approach is based on a time-domain formulation and analytic description of both reflections and diffractions. Thus, the method has the same limitations as for time migration: locally the lateral velocity variations cannot be too large.

In 2D, two CRS parameters are needed to characterize diffractions. One of these parameters is closely related to the NMO-velocities, whereas the other one contains curvature information. In this thesis we have introduced a simple parametric relationship between the two CRS parameters generalized to a layered medium including possible dips. This implies a more efficient search for the optimal CRS parameters.

The separation technique has been applied to two synthetic datasets. The first set of data was used to analyze the basic difference between diffractions and reflections when viewed in various data domains. Based on such observations a good strategy could be proposed to separate the diffractions. To evaluate the performance of the modified CRS-technique it was then applied to a complex synthetic dataset, Sigsbee2a. This set of data includes a rough salt body and its boundary was expected to generate substantial diffracted energy. A successful diffraction separation was obtained using the CRS method. In addition, a method to detect the apex of a scatterer was introduced and used to generate a map of the scatterer (alternative to imaging). This map gave a good description of the boundary of the salt.

In this study, only a ZO-type of formulation has been used. Further use of the method should investigate the extension to an arbitrary offset case. Also, a more systematic analysis of the sensitivity of the technique to model complexities should be in focus of future work.

REFERENCES

ASGEDOM, E. G., GELIUS, L. J., AUSTENG, A. & TYGEL, M. 2011 b. A new approach to post-stack diffraction separation. *SEG Expanded Abstracts* 30.

ASGEDOM, E. G., GELIUS, L. J., FACCIPERI, J. H. & TYGEL, M. 2012. 2-D pre- and post-stack diffraction separation and imaging. *SEG Extended Abstract*.

ASGEDOM, E. G., GELIUS, L. J. & TYGEL, M. 2011 a. Diffraction separation using the CRS technique: A Field data application. *Expanded Abstrat,Twelfth International Congress of the Brazilian Geophysical Society*.

ASGEDOM, E. G., GELIUS, L. J. & TYGEL, M. 2011 c. Higher-Resolution Determination of Zero-Offset Common-Reflection-Surface Stack Parameters. *International Journal of Geophysics,* 2011.

FOMEL, S. 2002. Applications of plane-wave destruction filters. *Geophysics,* 67**,** 1946-1960.

FOMEL, S., LANDA, E. & TANER, M. T. 2007. Poststack velocity analysis by separation and imaging of seismic diffractions. *Geophysics,* 72**,** U89-U94.

GELIUS, L. J. & JOHANSEN, T., A. 2010. *Petroleum Geophysics,* Published by, Unigeo as.

GIBSON, B., LARNER, K. & LEVIN, S. 1983. Efficient 3-D migration in two steps. *Geophysical Prospecting,* 31**,** 1-33.

JAGER, R., MANN, J., HOCHT, G. & HUBRAL, P. 2001. Common-reflection-surface stack: Image and attributes. *Geophysics,* 66**,** 97-109.

KANASEWICH, E. R. & PHADKE, S. M. 1988. Imaging discontinuities on seismic sections. *Geophysics,* 53**,** 334-345.

KHAIDUKOV, V., LANDA, E. & MOSER, T. J. 2004. Diffraction imaging by focusing-defocusing: An outlook on seismic superresolution. *Geophysics,* 69**,** 1478-1490.

KIRLIN, R. L. 1992. The relationship between semblance and eigenstructure velocity estimators. *Geophysics,* 57**,** 1027-1033.

LANDA, E., SHTIVELMAN, V. & GELCHINSKY, B. 1987. A method for detection of diffracted waves on common-offset sections. *Geophysical Prospecting,* 35**,** 359-373.

LEVIN, F. K. 1971. Apparent velocity from dipping interface reflections. *Geophysics,* 36**,** 510-516.

MANN, J., SCHLEICHER, J. & HERTWECK, T. 2007. CRS stacking - A simplified explanation. *EAGE 69th Conference & Technical Exibition - London, UK*.

MONDOL, N. H. 2010. Seismic Exploration. *In:* BJORLYKKE, K. (ed.) *Petroleum Geoscience: From Sedimentary Environments to Rock Physics.* Springer-Verlag Berlin Heidelberg.

MOSER, T. J. & HOWARD, C. B. 2008. Diffraction imaging in depth. *Geophysical Prospecting,* 56**,** 627-641.

PAFFENHOLZ, J. 2001. Sigsbee2 synthetic subsalt dataset: image quality as function of migration algorithm and velocity model error, workshop "Velocity Model Independent Imaging in Complex Media". *71st Ann. Internat. Mtg., Soc. Expl. Geophys.*

RICKER, N. 1953. The form and laws of propagation of seismic wavelets. *Geophyscis,* 18**,** 10-40.

ZHANG, Y., BERGLER, S. & HUBRAL, P. 2001. Common-reflection-surface (CRS) stack for common offset. *Geophysical Prospecting,* 49**,** 709-718.

http://www.reproducibility.org/data/sigsbee/ Last accessed 24th May, 2012.